

RESEARCH ARTICLE | NOVEMBER 01 2023

Partially saturated granular flow in a rotating drum: The role of cohesion

Mingrui Dong ; Zhongzheng Wang ; Benjy Marks ; Yu Chen ; Yixiang Gan  



Physics of Fluids 35, 113302 (2023)

<https://doi.org/10.1063/5.0166241>



View
Online



Export
Citation

CrossMark



APL Quantum
Bridging fundamental quantum research with technological applications

Now Open for Submissions
No Article Processing Charges (APCs) through 2024

Submit Today



Partially saturated granular flow in a rotating drum: The role of cohesion

Cite as: Phys. Fluids **35**, 113302 (2023); doi: 10.1063/5.0166241

Submitted: 4 July 2023 · Accepted: 13 October 2023 ·

Published Online: 1 November 2023



View Online



Export Citation



CrossMark

Mingrui Dong,¹ Zhongzheng Wang,² Benjy Marks,¹ Yu Chen,¹ and Yixiang Gan^{1,3,a)}

AFFILIATIONS

¹School of Civil Engineering, The University of Sydney, Camperdown, NSW 2006, Australia

²School of Mechanical, Medical and Process Engineering, Faculty of Engineering, Queensland University of Technology, Brisbane, QLD 4001, Australia

³Sydney Nano, The University of Sydney, Camperdown, NSW 2006, Australia

^{a)} Author to whom correspondence should be addressed: yixiang.gan@sydney.edu.au

ABSTRACT

Partially saturated granular flows are common in various natural and industrial processes, such as landslides, mineral handling, and food processing. We conduct experiments and apply the discrete element method to study granular flows in rotating drums under partially saturated conditions. We focus on varying the strength of cohesion (surface tension) and rotation rate within the modes of rolling flow and cascading flow. With an increase in surface tension, a rolling mode can possess a steeper slope and correspondingly needs a higher rotation rate to transition to a cascading. The depth of the flowing region increases with increasing cohesion, while the sensitivity is reduced for cases of high cohesion. We propose a dimensionless number C_E that captures the combined effects of rotation, gravity, and cohesion on the dynamic angle of repose and flow depth. In addition, we extract statistical information on the formation of clusters within the flow. We find a power law relation between the cluster size distribution and its probability, which indicates that stronger cohesion can promote the formation of larger clusters, and we discuss how cohesion impact on flows manifested by cluster formation.

Published under an exclusive license by AIP Publishing. <https://doi.org/10.1063/5.0166241>

I. INTRODUCTION

Granular materials are prevalent in all domains of human activity, from natural sands to industrial and mining operations.¹ When disturbed, these materials can transition from behaving as a solid to flowing like a liquid. The rheological properties of this flowing material have been studied under various conditions.^{2–6} Individual grains in these flows can be characterized by properties, such as their size, shape, and mass. A granular flow, when described as a continuum, can alternatively be described by fields, such as the density (or solid fraction), pressure, and strain rate. To determine the relationships between the individual particle properties and their continuum equivalents, many apparatus and simulations with different geometries have been studied for granular media with and without the presence of inter-particle cohesion.^{2–4,7–14} However, there is still a lack of comprehensive understanding of the flow behavior of cohesive granular materials.

A granular surface flow can occur due to the presence of gravity and a difference in height. A surface flow is characterized by a flowing layer of grains at the surface, with stationary grains underneath. Surface particles flowing along steeper slopes tend to possess higher velocities.¹⁵ For slightly cohesive particles under the same conditions,

surface particle velocity is observed to be reduced.¹⁴ With the increase in cohesion, the surface flow can transition to a plug flow, where a plug region can be found overlying a shear band.^{7,10,16} The stratification of the flow region can be viewed as a transition from a collisional flow to a viscoplastic regime.^{10,17,18} A viscoplastic flow can be characterized as a shear rate sensitive regime that shear resistance can rise corresponding to the tendency of an increasing shear rate, while the shearing strength is less affected by a varying shear rate in a collisional flow regime. Therefore, the critical conditions between these two regimes can be reflected in the change in along-depth velocity and strain rate profiles, and flow layer depth. The variation of the flowing layer depth, i.e., the distance between the flow surface and the flow-solid interface, may indicate the dissipation of the amount of gravitational energy that was previously stored by particles flowing on the top.^{14,19}

Since characteristic particle size plays a crucial role in affecting various aspects of granular flow, including inter-particle friction, packing and porosity, permeability and seepage, segregation and mixing,^{20–23} a description of the cluster formation can be critical.^{11,15,24} It is particularly useful to understand the flow mechanism of cohesive

particles.^{3,7,15,18,25} Bonamy *et al.*²⁶ studied cluster formation in cohesionless particle surface flows based on velocity fluctuations, where a negative power law relation was identified between the cluster size (quantified by the number of particles within a cluster) and their corresponding probabilities. Cao *et al.*²⁵ demonstrated that the inter-cluster plastic rearrangement between unstable tetrahedral clusters plays an essential role in the plasticity of sheared granular materials. Zou *et al.*²⁷ presented how the particle shape (aspect ratio) can contribute to increasing the cluster formation in a dense granular flow. For cohesive particles, a viscoplastic flow accompanied by free surfaces that possess repetitive patterns due to the formed clusters can be observed.¹⁸ The velocity of intra-cluster particles remains coherent, which can lead to a relatively low local granular temperature.¹⁴ Rognon *et al.*⁷ mentioned that clusters can play a key role in the dilation effect of cohesive granular flows.

The rotating drum has been widely used in various applications and provides rich information on granular flow.^{4,5,11–14} Particles in a rotating drum can be divided into two parts. First, a passive, “solid-like,” region is rotated along the tube before flowing down. Second, an active flow, “fluid-like,” region forms a surface flow. As the rotation rate increases for a given granular medium, the flow can be characterized into six surface flow modes: slipping (no flow), slumping (intermittent avalanches), rolling (continuous flow with a tilted flat surface), cascading (continuous flow with a curved “S” shape surface), cataracting (overturning tumbling), and centrifuging (all particles stuck to the tube walls).²⁸ It has been shown that the transition between these modes depends on a variety of parameters, e.g., the rotation rate, particle shape, particle-to-drum size ratio, filling rate, wall effects, and cohesion effects.^{14,29–33} The dimensionless Froude number (Fr) is widely adopted to describe the mode transition,

$$Fr = \sqrt{\omega^2 R/g}, \quad (1)$$

where ω is the rotation rate, R is the drum radius, and g is the gravitational acceleration. The Froude number considers the competing effects of inertia and gravity.^{14,31} A low Froude number typically corresponds to slipping, and a Froude number greater than one represents centrifuging. In this work, unless stated otherwise, we focus on flow transition between rolling and cascading flow modes. Within the rolling and cascading modes, the dynamic angle of repose θ is a critical parameter for characterizing the behavior of the granular flow.^{14,28,34,35} A relationship between Fr and the dynamic angle of repose can be established,^{31,36} where an increase in Fr can drive the transition gradually from slumping to rolling and then to cascading.

For cohesive particles in a rotating drum, two additional dimensionless numbers become relevant, namely, the Bond number (Bo), which describes the relative importance of cohesion compared to the gravitational force, and the Weber number (We), representing the ratio of inertia to cohesion.^{14,29} These two dimensionless numbers are expressed as

$$Bo = \frac{\gamma \cos \theta_C}{\rho g r_p^2}, \quad (2)$$

$$We = \frac{\rho r_p (\omega R)^2}{\gamma \cos \theta_C}, \quad (3)$$

where γ is the liquid surface tension, θ_C is the multiphase contact angle, ρ is the material density, r_p is the average particle radius, and ω

is the rotation rate. Within relatively high cohesion, typically, the $Bo > 1$, intermittent avalanches can be observed when the rotating rate is low.³⁷ While under the same condition, a continuous flow can be found for cohesionless particles.²⁹ Within continuous flow modes, a nonlinear correlation can be found between We and the dynamic angle of repose.¹⁴

Here, we investigate the behavior of partially saturated granular media in a rotating drum through experimentally validated simulations with the discrete element method (DEM). We focus on quantifying and analyzing three key characteristic features: the dynamic angle of repose (θ), the flow depth (h), and the formation of clusters, under various rotation rates (ω) and surface tensions (γ). After the introduction, we first present the experimental setup and numerical method in Sec. II. In Sec. III, we discuss the effect of cohesion on these characteristic features to understand the relationship between cohesion energy (provided by γ) and kinetic energy (by ω). We propose a dimensionless number that takes gravity, inertia, and cohesion into account and demonstrate its effectiveness in characterizing cohesive granular flows in a rotating drum. Finally, we discuss the implications of our findings and conclude with potential research directions.

II. METHOD

A. Rotating drum setup

A photograph of the experimental apparatus is shown in Fig. 1. The sidewalls of the rotating drum are fabricated from clear acrylic. The drum body is 3D printed polylactic acid thermoplastic (density 1.24 g/cm³) using an Ultimaker3 3D printer. Twelve bulges are spaced evenly around the drum to prevent slip between particles and the drum. The bulges are cylindrical with diameter $2r_p$, which ensures that their effect on the flow behavior in bulk regions is negligible.^{38,39} The system is made watertight with a sealing strip between the drum and the sidewalls. Two nonstick and transparent FEP fluoropolymer films (with low surface energy leading to a contact angle of around 100°) are attached to the sidewalls to prevent wet particles from sticking to them. Glass beads with average radius $r_p \approx 1.01 \text{ mm} \pm 3\%$ are used. A high-speed camera shooting at a frame rate of 500 fps with 1920 × 1080 pixels is used to capture the granular flow through the transparent sidewalls. A LED ring light directed at the drum is set to provide enough light for the camera, and a blackboard is attached to the back of the drum to act as a homogeneous contrasting background. At this zoom level, each particle is approximately 8 × 8 pixels, which ensures precision of the experimental results.

The filling level of the drum is expressed as $\frac{V_{\text{filled}}}{V_{\text{container}}} \approx 30\%$, where a total of 376.6 g of glass beads in the experiment is used. We study here low volumetric water content conditions, i.e., $m_w = V_{\text{liquid}}/V_{\text{solid}} \leq 2\%$, where V_{liquid} is the volume of liquid and V_{solid} is the volume of solids. In this state, the liquid exists mainly in the form of liquid bridges in the granular materials, which creates attractive inter-particle (capillary) forces and consequently impacts the behavior of the granular medium.^{40–42} In this study, we consider the capillary force supplied by the liquid bridge as the primary source of this cohesion effect, which is the case for particles of size greater than $\sim 100 \mu\text{m}$ where van der Waals force can be neglected.^{40,43} In the experiment, 3.1 ml of distilled water is added to make $\approx 2\%$ volumetric water content in the experiment to ensure a pendular state, which possesses a typical surface tension $\approx 0.073 \text{ N/m}$ under a room temperature.

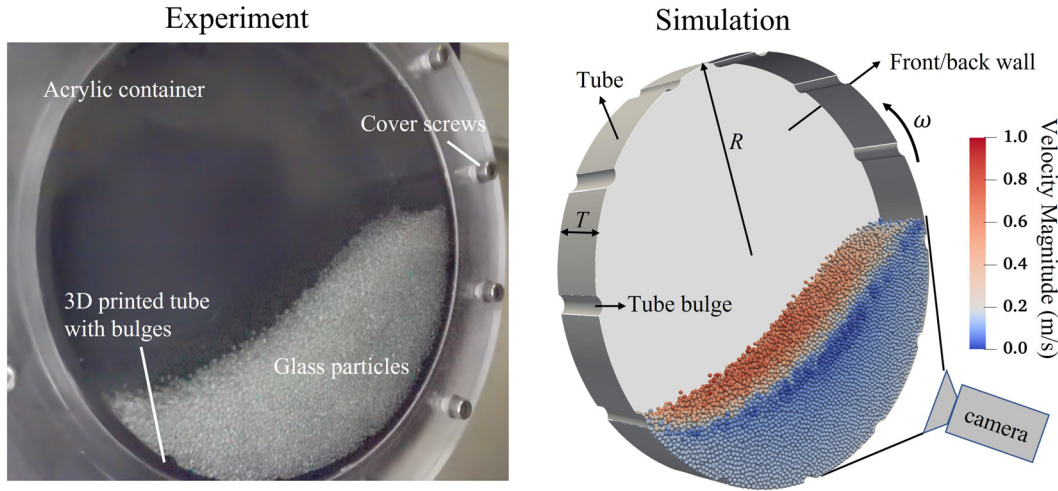


FIG. 1. The experiment and simulation setup. Left: a photo of the experimental rotating drum with a rotation rate $\omega = 15$ rpm under dry conditions. Right: a simulation of the same scenario as the left experimental photo. The rotating drum has a radius R and depth T . Twelve bulges are used to avoid slipping between particles and the drum. The drum rotates anti-clockwise. The color scale from blue to red represents an increase in particle velocity magnitude.

A rendering of the simulation is shown in Fig. 1. We use a drum with internal radius $R = 96r_p$ and thickness $T = 30r_p$. 37 500 particles are used in the simulation to ensure the filling level is around 30%. The detail of the DEM modeling is explained in Sec. II B.

B. Discrete element method

The DEM has been proven to be effective in investigating granular phenomena with abundant detail.^{3,44–47} Here, we use the open-source platform LIGGGHTS to simulate the granular system.⁴⁸ The particle movement in DEM is described by the computation of Newton's second law. The normal, tangential, and rolling inter-particle contact laws are, respectively, described as^{49–51}

$$F_n^{\text{Hertz}} = k_n \delta_n - \beta_n \nu_n, \quad (4)$$

$$F_t = k_t \delta_t - \beta_t \nu_t, \quad (5)$$

$$M_r = k_r \Delta \theta_r - \beta_r \omega, \quad (6)$$

where n , t , and r represent the normal, tangential, and rolling directions, respectively, the superscript “Hertz” represents the Hertzian contact, F is the contact force, k is the contact stiffness, M is the rolling torque, δ is the overlap distance between contacting particles, $\Delta \theta_r$ is the relative rotation angle of contacting particles, β is the coefficient of damping, and ν and ω , respectively, denote the relative translational velocity and relative angular velocity for contacting neighbors. Here, k_n is expressed as the nonlinear Hertzian law by $k_n = \frac{4}{3} E \sqrt{R^* \delta_n}$, where E is the Young's modulus and $R^* = \frac{r_i r_j}{r_i + r_j}$ is the effective radius of contacting neighbors. The tangential friction force and rolling torque, F_t and M_r , are capped to satisfy a Coulomb style criteria defined by $|F_t| \leq \mu_s |F_n^{\text{total}}|$ and $|M_r| \leq \mu_r r_p F_n^{\text{total}}$, respectively, where μ_s is the coefficient of sliding friction and μ_r is the coefficient of rolling friction.⁵⁰ Notice that μ_s for glass beads can vary from 0.2 to 0.65,^{52–56} we select $\mu_s = 0.5$ in this study, a common value adopted in the literature.^{52,53}

The choice of the appropriate coefficient of restitution e for granular flows is an active area of research. Experiments have indicated that greater collisional velocity corresponds to smaller e .⁵⁷ For cohesive granular flows, e can drastically decrease even at low impact velocity.^{58,59} Furthermore, for particle collisions submerged in surrounding fluids with viscosity that cannot be ignored, e also decreases with the Stokes number that reflects the ratio of particle inertia to particle viscous drag.⁶⁰ At lower levels of water content, the liquid is localized near the contacts (as capillary bridges), and the dissipation mechanisms include the viscous effect and the hysteretic effect from the forming and breakup of capillary bridges.⁶¹ Thus, the choice of proper e depends on the relative dissipation to particle inertia. Here, we adopt a simplified approach of adopting a constant $e = 0.9$ to represent the effective coefficient of restitution, a common approach adopted in the literature.^{3,56,62} Computational stability^{44,47} is guaranteed by checking the time step $t = 10^{-8} \text{ s} \ll \sqrt{m/Ed_s} \approx 3 \times 10^{-7} \text{ s}$, where m denotes the mass of the smallest particle, $d_s = 0.95d_p$ denotes the diameter of the smallest particles, and particle size in this study is set uniformly distributed as $d_p = 2 \pm 5\%$. Table I lists key parameters adopted in this study.

C. The cohesion contact law

The constitutive model of capillary force proposed by Soulie *et al.*⁶³ is described by

$$F_n^{\text{cap}} = \pi \gamma \sqrt{r_i r_j} [c + e^{(a \delta_{\text{gap}} / r_j + b)}], \quad (7)$$

where F_n^{cap} is the normal capillary force, r_i and r_j are the radius of two neighboring particles linked by a liquid bridge with j indicating the larger one, δ_{gap} is the distance between the surfaces of each pair of neighboring particles, a , b , and c are coefficients deduced from the liquid bridge volume ($V_{\text{br}}^{\text{tri}}$), θ_C and r_p , respectively.⁶³ Here, the liquid film is assumed to fully cover the surface of particles, which leads to $\theta_C = 0^\circ$.⁶⁴ Note the lubrication effect is considered negligible in this study due to the adopted low water content and kinetic viscosity,

TABLE I. Model parameters.

Parameter	Value
Young’s modulus, E (Pa)	6×10^{10}
Coefficient of sliding friction, μ_s (-)	0.5
Coefficient of rolling friction, μ_r (-)	0.001
Coefficient of restitution (-)	0.9
Surface tension, γ (N/m)	0–0.146
Contact angle, θ_C ($^\circ$)	0
Gravitational acceleration, g (m/s ²)	9.81
Liquid dynamic viscosity, μ_v (Pa · s)	8.9×10^{-4}
Particle diameter, d_p (mm)	$2\% \pm 5\%$
Particle density, ρ (kg/m ³)	2460
Drum radius/depth, R/T (-)	$48d_p/15d_p$
Volumetric liquid content, m_w (-)	2%

which can avoid the build-up of interstitial hydrostatic pressure.^{34,65,66} A liquid bridge can form when the surface gap distance reaches $D_{\text{birth}} = h_{t,i} + h_{t,j}$, which takes the liquid film thickness $h_{t,i} = \sqrt[3]{V_i^{\text{solid}} + V_i^{\text{liquid}}} - r_i = 0.007r_i$ into consideration. The liquid bridge rupture distance $D_{\text{rupture}} = (1 + 0.5\theta_C) \times (V_{ij}^{\text{bri}})^{\frac{1}{3}}$ is adopted, beyond which the liquid bridge breaks, and F_n^{cap} no longer exists.⁶⁷ Based on the assumption $m_w \leq 2\%$, the liquid volume on each particle is set as $V_i^{\text{liquid}} = V_i \times 2\%$, where V_i denotes the volume of the particle i . The liquid bridge volume V_{ij}^{bri} is calculated as $0.05 \times (V_i^{\text{liquid}} + V_j^{\text{liquid}}) = (V_i + V_j) \times 0.1\%$, where the coefficient 0.05 ensures liquid volume conservation when contacting neighbors of each particle may reach 12 (face-centered-cubic topological structure), meaning a maximum of 60% of the effective volumetric liquid content of one particle (V_i^{liquid}) forms liquid bridges. Note, the liquid weight plays a negligible role in the dynamics of particles since the mass ratio between liquid and particles is $\rho_l \times \frac{0.02}{\rho_p} \approx 2\%$. The particle-wall contact force is assumed to be the same as the particle–particle contact, with the wall side possessing an infinite radius to mimic a plate.^{30,68} A detailed illustration and analysis of the formation and rupture of the liquid bridges under different surface tensions can be found in our previous work.⁶⁹

III. RESULTS AND DISCUSSION

In this section, we first present the result of macro-scale phenomena, i.e., mode transition and dynamic angle of repose, in a parametric study by varying ω and γ . Through this process, the simulation is validated. After that, characterization indices of the meso-scale phenomena (flow depth) and the micro-scale phenomena (the size distribution of cohesion-induced clusters) are extracted. We propose a new dimensionless number to gain insight from these characteristic indices to discuss how cohesion affects the granular flow regime in the rotating drum.

A. Flow mode and dynamic angle of repose

We investigate the flow regime during the mode transition between rolling and cascading. Note the transition is evaluated through

visual observation results,^{5,70} and the curvature is not quantitatively examined. Both cohesionless (dry) and cohesive (wet) conditions under rotating speed $\omega = 15, 20,$ and 25 rpm are used to validate the simulation against the experiment. As shown in Fig. 2(a), comparing each of the cohesionless and cohesive cases indicates that the addition of cohesion results in a less curved slope (Cyan dashed lines) with respect to the cohesionless cases (Cyan solid lines). This shows that as ω increases, the cohesive case presents a delayed transition from rolling to cascading. That is, one needs a relatively higher ω to enable a rolling-cascading transition for cohesive particles than that for dry particles. An uplifted slope toe of the cohesionless condition can be used to distinguish it from the cohesive case, which is highlighted by red circles in Fig. 2(a). A further increase in cohesion can lead to a flattened profile, which was observed in previous studies^{14,68,71} and will also be presented in Sec. III B.

To quantitatively capture the differences in surface profiles under different cohesion and rotation rate, the dynamic angle of repose (θ) is extracted. As illustrated in the top left inset of Fig. 2(a), a coordinate can be constructed taking the red dot as the origin located on the surface with the x^{local} axis points toward the right, and an angle between the slope and x^{local} can be obtained. When the red dot moves along the slope from the toe to the top, a variation of θ can be found. Here, unless stated otherwise, a maximum value of θ , representing the steepest point for the free surface slope, is defined as the dynamic angle of repose.^{14,35,36} Note the definition of θ is the same in both experiments and simulations. The θ is plotted against the inverse of We in Fig. 2(b). The θ_C which can be affected by surface roughness, materials type, and sphericity, is assumed as $\approx 60^\circ$ in the experiment based on previous studies.^{42,72} The relation between θ and the inverse of We shows a sharp increase at low cohesion cases followed by a near plateau at high cohesion, which is consistent with previous work.¹⁴ Moreover, in Fig. 2(b), we can see that either an increase in cohesion or rotation rate can lead to a higher θ .

Small discrepancies between simulation and experiments can be attributed to two reasons. In simulation, the particle–wall interaction is assumed to be identical to inter-particle contact with the wall side possessing an infinite radius to mimic a plate. However, a weaker particle–wall interaction may cause less energy dissipation in the experiment. Additionally, although liquid and particles are fully mixed before filling into the drum, the difference in liquid distribution between the experiment and simulation may cause differences in particle cluster formation, which will be discussed in Sec. III C.

To measure the impact of the cohesion and the rotation rate on θ , we discuss the influencing factor separately. First, we focus on the variation of θ under a cohesion-dominant condition. Nowak *et al.*²⁹ examined low rotation rate in the slumping mode with intermittent avalanches. Under this cohesion-dominant condition, the maximum static angle of repose could be correlated with the cohesion strength through force balance, leading to the relationship,²⁹

$$\max(\theta_{\text{stat}}) - \min(\theta_{\text{stat}}) \propto \sqrt{\left(\frac{9\pi}{2\phi}\right)^{\frac{1}{2}} \left(\frac{\alpha \cos(\min(\theta_{\text{stat}}))\gamma}{\sqrt{6} \tan(\min(\theta_{\text{stat}}))\rho g r_p L}\right)}, \tag{8}$$

where $\max(\theta_{\text{stat}})$ is the maximum static angle of repose, which is not affected by the rotating speed, $\min(\theta_{\text{stat}})$ is the averaged minimum static angle of repose that can balance particles weight on a slope, ϕ is

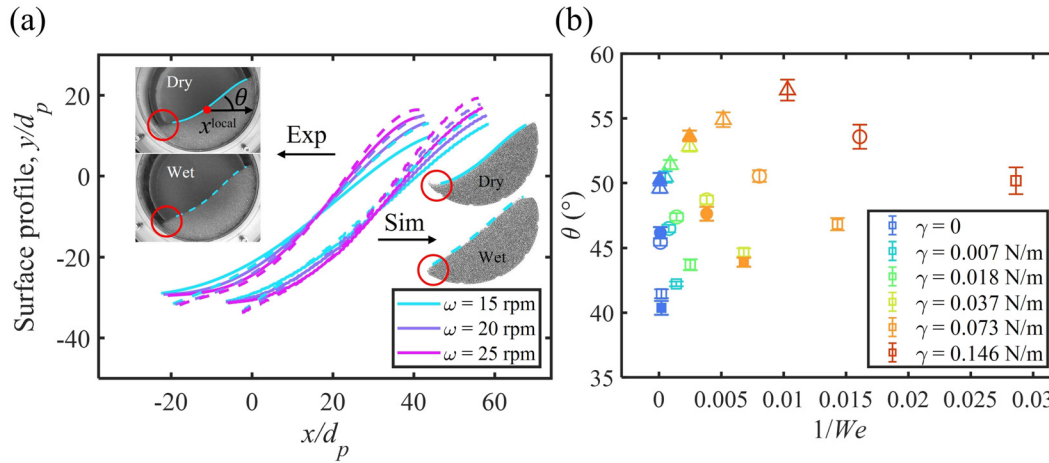


FIG. 2. (a) Surface profiles of experiments (left lines) and simulations (right lines). Solid lines represent dry conditions, and dashed lines wet (cohesive) conditions. Insets at the left show two photographs of the experiment under dry and wet conditions. As a comparison, the right insets show two renderings of simulations under the corresponding conditions to the left insets. Note a slight difference in the filling level (volumetric particle content) between experiments ($29.7\% \pm 0.6\%$) and simulations (30.2%) can be the reason that profiles less ideal intersect. Moreover, axes centers for both experiments and simulations (Sim) should be identical; however, a shift toward the left is applied to the Sim cases to observe the profile clearly. Red circles highlight the difference in slope toes between cohesive (flattened) and dry (curved) conditions. See the detailed description of how the dynamic angle of repose θ is defined in Sec. III A. (b) The dynamic angle of repose θ as a function of $1/We$. Hollow markers are simulation results, and solid markers are experimental results. \square , \circ , and \triangle represent $\omega = 15, 20$, and 25 rpm, respectively. The error bar of the experiment results is calculated from the standard deviation of five repeating cases. The error bar of simulations is obtained as the standard deviation of more than ten θ datasets recorded along every 0.25 revolution after the dynamic angle of repose reaches a steady state.

the solid packing fraction, α is a constant coefficient, r_p is the particle radius, and L is a constant representing a characteristic system size. This equation describes a linear relationship between the maximum static angle of repose with surface tension. Given the definition of Bond number in Eq. (2), Eq. (8) can be further simplified to

$$\max(\theta_{\text{stat}}) - \min(\theta_{\text{stat}}) \propto Bo^{1/2}, \quad (9)$$

implying a linear relationship between the increase in the static angle of repose and $Bo^{1/2}$. Figure 3(a) shows the linear relation between $Bo^{1/2}$ and θ with different rotation rates.

At higher relative rotation rates, when inertial effects become dominant, it has been observed that the flow becomes continuous, and the Fr can be adopted to evaluate the dynamic angle of repose,¹⁴ which can be expressed as

$$\theta - \theta_{\text{fit}} \propto Fr, \quad (10)$$

where $\theta_{\text{fit}} \approx 22^\circ$ is a fitting parameter.¹⁴ Here, Eq. (10) also indicates a linear relation between the increase in dynamic angle of repose and Fr , which can be seen in Fig. 3(b).

It can be seen that Eqs. (8) and (10) independently take the effects of cohesion and inertia on θ into account, respectively. Whereas in the current system, both cohesion and inertia effects are considered, as such, it is expected that both Fr and Bo should impact the resulting θ .

To take both the cohesion and inertial effects into account, based on Eqs. (8) and (10), we define a new non-dimensional parameter C_E as

$$C_E = Bo^{1/2} + \lambda \cdot Fr, \quad (11)$$

where C stands for ‘‘Combination’’ and E represents ‘‘Effects of rotation, gravity, and cohesion.’’ Then, assuming a linear relationship

based on the observation from Figs. 3(a) and 3(b), the angle of repose can be quantitatively estimated by

$$\theta_{\text{pred}} = \theta_1 \cdot C_E + \theta_2, \quad (12)$$

where θ_1 , λ , and θ_2 are fitted to be 6.47° , 12.25° , and 28.29° , respectively, with a goodness of fitting $R^2 \approx 0.98$. Using Eqs. (11) and (12), we can see θ agrees well with θ_{pred} in Fig. 3(c). Note the slight modification of Eqs. (8) and (10) when they are combined to form C_E . In Eq. (8), $\min(\theta_{\text{stat}}) \approx 23.8^\circ$ is a theoretical parameter that is independent of systems.²⁹ As a result, θ_1 and λ represent the sensitivity of θ on $Bo^{1/2}$ and Fr , respectively, and combined with θ_2 (a system-dependent fitting coefficient), they can be looked as the reformatted fitting coefficient for capturing both $\min(\theta_{\text{stat}})$ and θ_{fit} .

B. Flow depth

Underneath the surface, the particle assemblies can be divided into flow and solid regions based on the index that depicts the local flow (deformation) with respect to time, i.e., shear strain rate $\dot{\epsilon}_s$. Here, $\dot{\epsilon}_s$ is expressed as $\dot{\epsilon}_s = \frac{1}{2}(\frac{\partial v_x}{\partial y} + \frac{\partial v_y}{\partial x})$, where v_x and v_y are time-series averaged local velocities (mapped in mesh grids with a size $2d_p$) along the x and y axes, and ∂ is the differential operator. The shear strain rate for varying cohesion and rotation rate are shown as a phase diagram in Fig. 4. A critical value $\dot{\epsilon}_{s,\text{crit}} = 10 \omega$ is applied to indicate the flow-solid interface, which is shown as black solid lines in the rendering of all cases in Fig. 4.

Within the flow region, a relatively high $\dot{\epsilon}_s$ area in the lower part of the slope can be observed when cohesion is not dominant. As a comparison, a relatively high cohesion tends to split the flow region into a plug zone overlying a shear band^{7,10,18} (Fig. 4, $We = 70$).

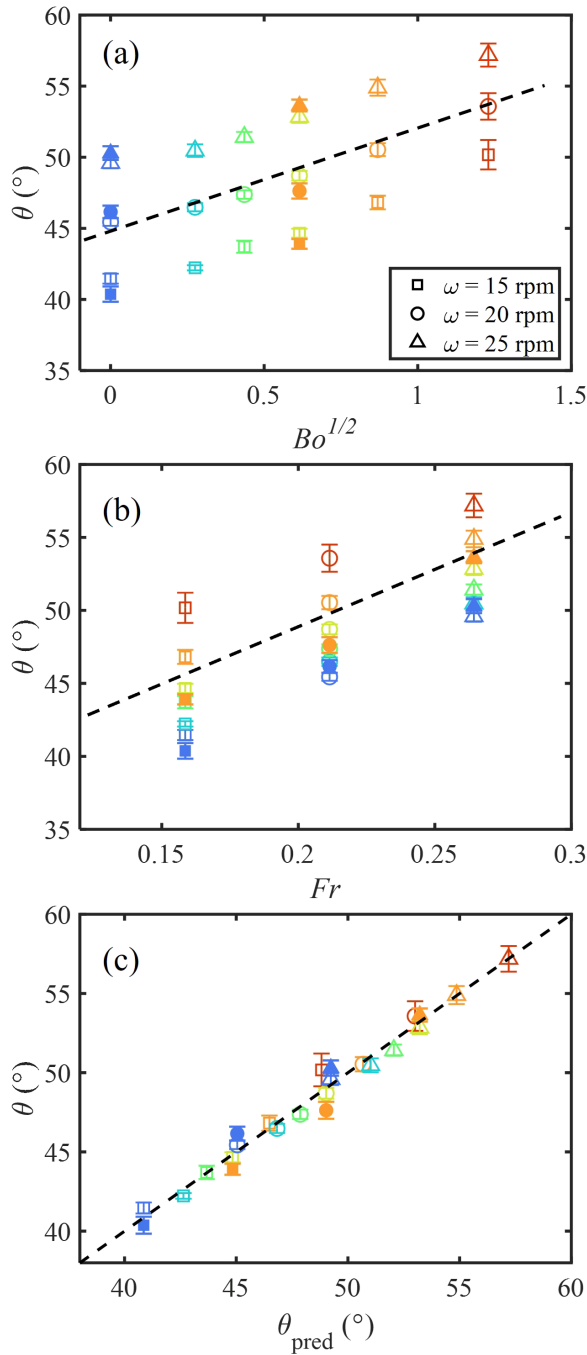


FIG. 3. Variation of the dynamic angle of repose as a function of (a) $Bo^{1/2}$, (b) Fr , and (c) C_E . Dashed lines in (a) and (b) are the guide for eye of linear relationships, and in (c) indicates $\theta = \theta_{pred}$. Color transitions from blue to red indicate an increase in cohesion, see Fig. 2(b).

The variation of flow region can be attributed to the transition from a collisional regime to a viscoplastic regime due to the increase in cohesion. Within the collisional regime, particles possess relatively high velocities [shown as the velocity profile in Figs. S1(a), S1(d), and S1(g)]

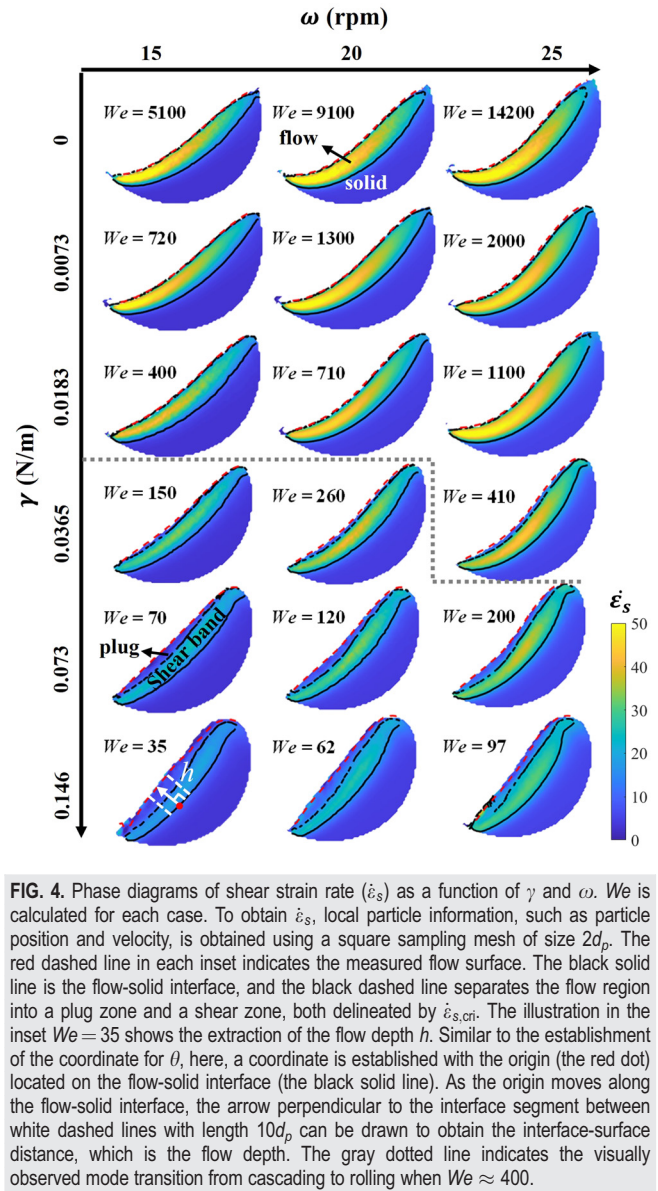


FIG. 4. Phase diagrams of shear strain rate ($\dot{\epsilon}_s$) as a function of γ and ω . We is calculated for each case. To obtain $\dot{\epsilon}_s$, local particle information, such as particle position and velocity, is obtained using a square sampling mesh of size $2d_p$. The red dashed line in each inset indicates the measured flow surface. The black solid line is the flow-solid interface, and the black dashed line separates the flow region into a plug zone and a shear zone, both delineated by $\dot{\epsilon}_{s,cri}$. The illustration in the inset $We = 35$ shows the extraction of the flow depth h . Similar to the establishment of the coordinate for θ , here, a coordinate is established with the origin (the red dot) located on the flow-solid interface (the black solid line). As the origin moves along the flow-solid interface, the arrow perpendicular to the interface segment between white dashed lines with length $10d_p$ can be drawn to obtain the interface-surface distance, which is the flow depth. The gray dotted line indicates the visually observed mode transition from cascading to rolling when $We \approx 400$.

while moving along the depth since little energy can be dissipated through collisions. The velocity profiles also show a slower decreasing trend of velocity from the surface as the cohesion increases, which are captured as the corresponding variation of the strain rate profile in Figs. S1(b), S1(e), and S1(h). Additionally, the flow region is eroded by the solid region because particles near the flow-solid interface are trapped in the solid region, which narrows the flow region near the toe. The combination of relatively high velocity and narrowed flow region leads to a higher temporal deformation, i.e., high $\dot{\epsilon}_s$, near the toe of slopes. In contrast, for the viscoplastic regime, relatively low $\dot{\epsilon}_s$ either in the plug zone or the localized shear band shows that the temporal deformation of particles is constrained by the cohesion due to the stronger energy dissipation.

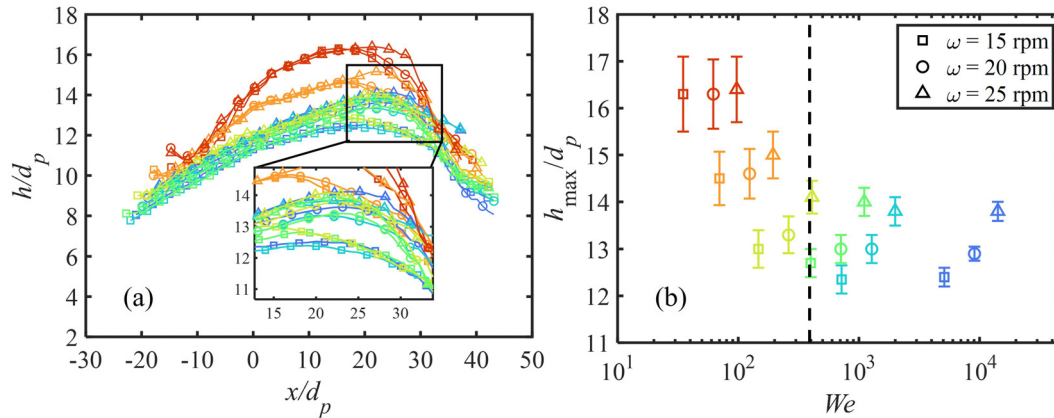


FIG. 5. (a) The flow depth h scanning along the x (horizontal) direction, which is illustrated in the inset ($\omega = 15$ rpm and $\gamma = 0.146$ N/m) of Fig. 4. The inset shows the area in the square for clarity. (b) The max flow depth h_{max} is plotted as the function of We . Color transitions from blue to red indicate an increase in cohesion, which can be referred to Fig. 2(b). The dashed line shows a critical value of $We = 400$.

A flow depth h can be extracted as the distance from the flow surface (red dashed lines) to the interface (solid lines), as illustrated in Fig. 4, case $We = 35$. The flow depth (h) is plotted along the x axis shown in Fig. 5(a). The concave shape of h depicts the inhomogeneity of the flow region observed in Fig. 4, which is an intrinsic feature of rotating drums.^{3,8} The maximum flow depth h_{max} , as a meso-scale index, is plotted against We in Fig. 4(b).

Interestingly, both cohesion and rotation rate possess a positive linear relationship with θ , whereas flow depth is less affected by rotation rate as cohesion increases. This may be attributed to that as cohesion increases, the solid region can possess higher strength and reach a higher peak, meaning higher gravitational potential is accumulated. Thus, when the solid region is sheared to fail and flow down, more energy needs to be dissipated compared to less cohesive cases. In Fig. 4, the flow region

with smaller ϵ_s due to the dominance of capillary force implies a less intensive deformation, meaning the increased inter-particle bonds can enhance energy dissipation in the flow region.⁷³ Therefore, greater h_{max} is observed when the Weber number is small, indicating the viscoplastic regime (cohesion-dominated regime), and it is insensitive to inertial effects, i.e., h_{max} remains similar, and ω has little effect. As We increases, the flow then gradually enters the collisional regime (inertia-dominated regime), where h_{max} becomes less relevant to the cohesion force.

C. Cluster formation

The discrete nature of granular flow makes it complex and challenging to characterize.^{1,75} Clusters can form in granular flows, which can make the energy dissipation in the flow region more complex.^{7,25}

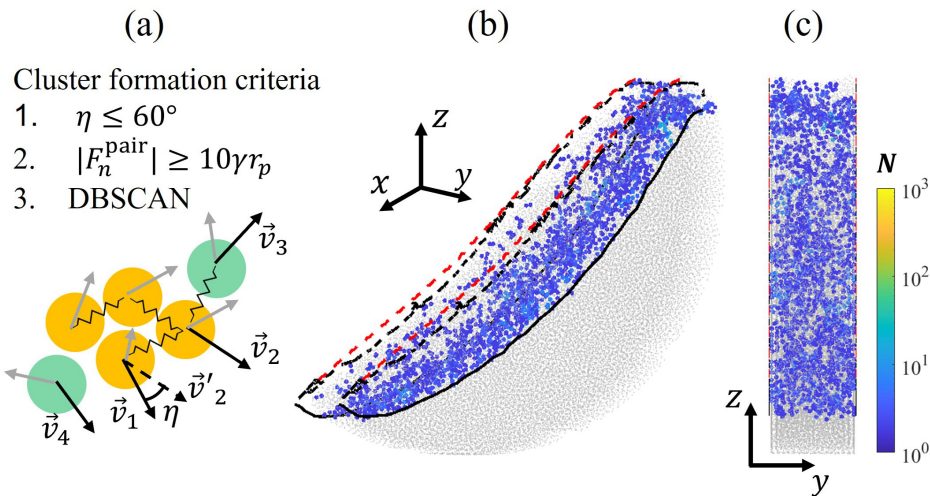


FIG. 6. Cluster formation criteria and an illustration example of clusters formed in granular flow. (a) The cluster formation criteria and illustrations. η is the angle between the vector of fluctuation velocity (black arrows) of each pair of neighbors. Gray arrows depict the true velocity of each particle. The spring between particles represents the normal contact force F_n^{pair} . The DBSCAN algorithm is adopted using MATLAB toolbox, which was developed by Ester *et al.*⁷⁴ Yellow circles indicate the formed clusters, and the greens are single particles. (b) and (c) show two 3D perspectives of one example of cluster formation in wet granular flow. Red circles circulate four cluster locations. The red dashed line, black dashed line, and black solid line are flow surface and ϵ boundaries the same as the case in Fig. 4 with $\omega = 15$ rpm and $\gamma = 0.037$ N/m.

Here, we first introduce our cluster formation criteria modified based on previous research, followed by discussions on cluster spatial information, cluster size distribution, and the relationship with flow mechanisms.

Based on the concept of velocity fluctuation, inter-particle contact, and inter-particle displacement, several methods have been used to characterize cluster formation.^{11,24,27,76} Given that cohesion is essential regarding inter-particle constraints, we adopt particle-level indices extracted from velocity fluctuation and inter-particle contact force to investigate cluster formation in the cohesive granular flow [see illustration in Fig. 6(a)]. The translational granular temperature diagram (see Fig. S2 in the supplementary material) shows the intensity of inter-particle relative movement (described by T_g) due to the increased cohesion. It can also be found that as the cohesion increases, the areas possessing less intensity of T_g appear first near the surface. By taking these two factors into consideration, we aim to extract particles that possess relatively higher normal interaction forces and similar moving directions, which guarantee a strong inter-particle bond and collective motion.

To implement the method, normal contact forces that meet the criteria $|F_n^{\text{pair}}| \geq 10\gamma r_p$ are classified as potential cluster participants. The effectiveness of a threshold around $10\gamma r_p$ is tested to capture the difference in cluster formation when cohesion is varying. The factor of ten used here is to set a contact force threshold significantly larger than that added effects from cohesion, isolating the major force network. The threshold of F_n^{pair} is important to identify cluster effects in cohesive granular materials as well as being the key to identify the cluster formation due to stronger connection. The scenario of defining F_n^{pair} a function of cohesion has already considered the importance of different levels of cohesion, from dry (in cases of $\gamma = 0$) to high cohesion cases.

To describe the spatial kinetic correlation among particles, the local velocity fluctuation is calculated for each particle as $\vec{v}_f = \vec{v}_i - v_m$, where i indicates the target particle and v_m is the corresponding local mean velocity. The local mean velocity is averaged by taking all particles, through accumulating more than a hundred-time steps, that locate in a sampling mesh grid into consideration. An angle η between each pair of $\vec{v}_{f,i}$ and $\vec{v}_{f,j}$ is calculated, and a critical angle $\eta_{\text{cri}} \leq 60^\circ$ is set to filter out non-correlated particles²⁶ [see Fig. 6(a)]. The DBSCAN algorithm is applied to construct clusters based on potential cluster participants screened by criteria η and F_n^{pair} . The DBSCAN algorithm sequentially searches for neighbors of a target particle to form clusters until no outside-cluster neighboring participants can be found, which can avoid relatively weak connections (single particle connection) among clusters.^{27,74}

A cluster formation illustration is shown in Fig. 6(a), where cluster particles are colored yellow, and single particles are colored green. A 3D view and a front view of the cluster formation example in the flow region of a simulation case ($\omega = 15$ rpm and $\gamma = 0.0365$ N/m) are shown in Figs. 6(b) and 6(c), respectively. The cluster formation under different cohesion and rotation rates is shown in Fig. 7, which illustrates that clusters occupy the region near the flow-solid interface in relatively fewer cohesive cases while spreading across the whole flow region in relatively strong cohesive cases. A reason for this can be that relatively weak cohesive contacts tend to develop near the surface region where no overburden pressure is applied. The weak contacts are easier to break, so clusters are rarely formed in that region. The

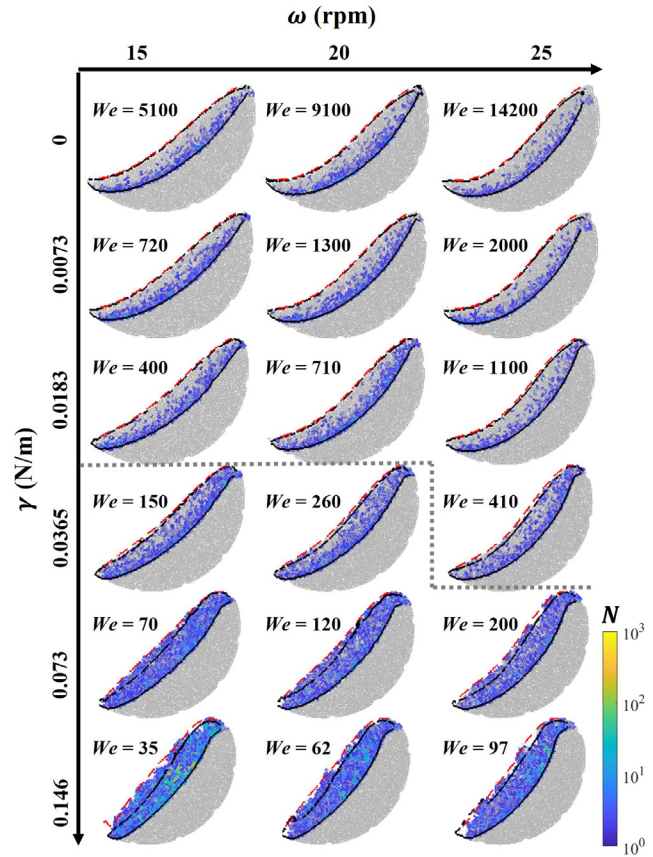


FIG. 7. Phase diagrams of cluster formation with varying cohesion and rotation rate. The color scale from blue to red indicates an increase in cluster size N .

packing fraction profiles along the depth in Figs. S1(c), S1(f), and S1(i) show a decrease in ϕ as cohesion rises, which reflects that the appearance of larger cohesive clusters can lead to low-density granular structures.⁶⁹

In strongly cohesive cases, it can be found that relatively large clusters appear mostly in the shear band (underneath the plug zone), which supports the view that the cluster formation in the shear band of cohesive granular materials is vital to resist shear.⁷ The appearance of clusters near the flow surface indicates the reason for a repetitive fluctuating surface profile shown in the corresponding plots of cases $We < 400$ in Fig. 7 and in work by Tegzes *et al.*¹⁸ Under this condition, an increase in rotation rate is found to have little effect on the cluster-occupied area and cluster sizes due to the cohesion-dominant mechanism.

Corresponding to the phase diagram of cluster formation in Fig. 7, the cluster size distribution of each case is plotted in Figs. 8(a)–8(c). A power law decay of the probability of cluster size $P(N) \propto N^{-\alpha}$ is found to be consistent with similar 2D and quasi-2D cases¹¹ with $\omega = 8$ rpm, where a smaller value of α indicates a greater chance of the formation of large clusters. For the cohesionless cases, the results by Bonamy *et al.*¹¹ together with our results show that a higher level of boundary constraints (from 3D to 2D) and a lower rotation rate (less kinetic

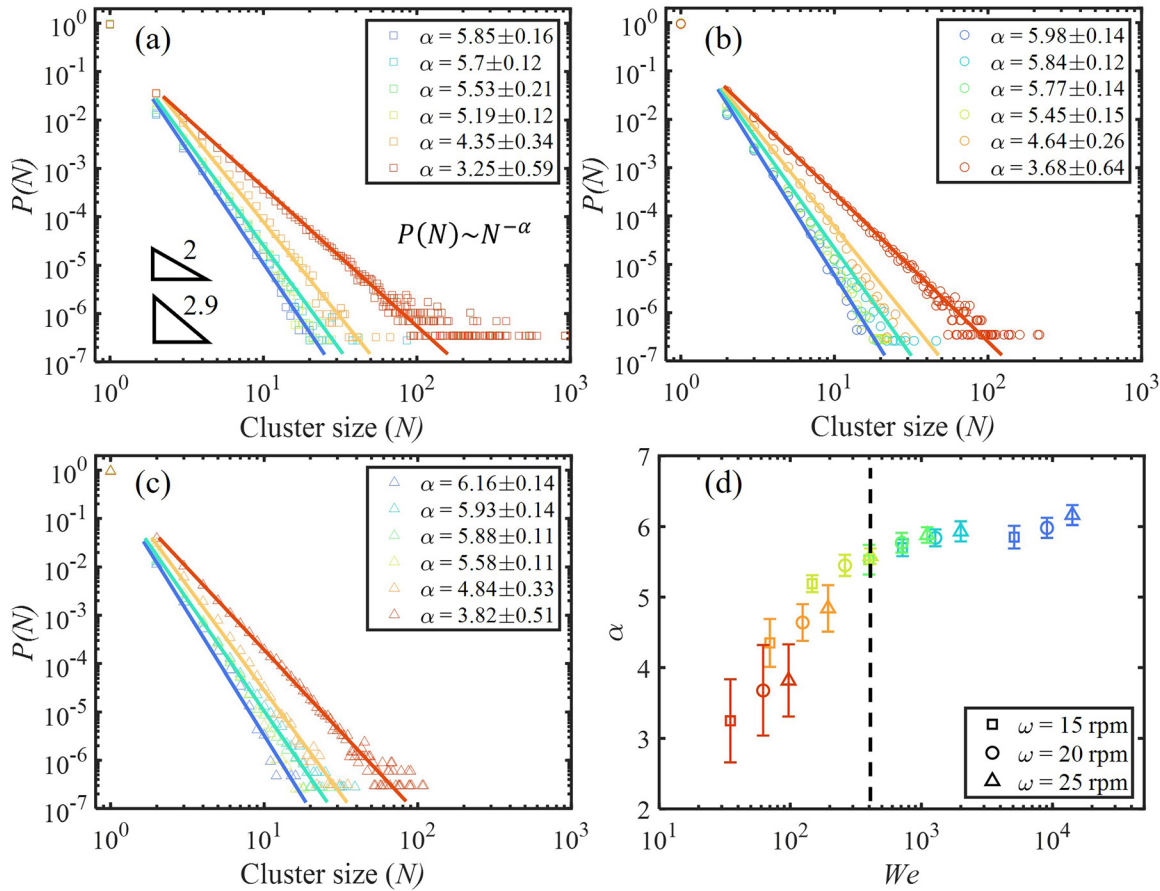


FIG. 8. Cluster size distribution. (a)–(c) The probability distribution (P) of cluster size (N). \square , \circ , and \triangle represent $\omega = 15, 20$, and 25 rpm, respectively. The color transition from blue to red indicates an increase in cohesion, which can be referred to Fig. 2(b). Solid lines are the guide of the eye for the power law relation shown in (a). Triangles in (a) indicate α slopes of the 2D ($\alpha = 2 \pm 0.1$) and quasi-2D ($\alpha = 2.9 \pm 0.1$) cases for mono-sized spherical particles under dry conditions in the work by Bonamy *et al.*¹¹ (d) The power index α is plotted as the function of We , where the color transition is consistent with (a)–(c).

energy) both make the flow tend to form larger clusters. This demonstrates that the velocity fluctuation can be constrained by more strict boundary confinement and lower inertia effects.^{15,24} As the cohesion rises, according to Figs. 8(a)–8(c), α decreases, implying a general increase in the size of formed clusters. We note that other factors such as can also impact the cluster size distribution, such as the coefficient of restitution and friction coefficient, which are interesting topics for future research. In particular, further exploring the effects of model parameters on the resulting cluster identification can be of interest to establish quantitative correlations between the mechanism and observation. Finally, α is plotted against We to describe the competing effect between cohesion energy and kinetic energy when observing cluster formation. Same as Fig. 5(b), the result shows that $We \approx 400$ is a critical value above which the effects from cohesion on cluster size become negligible.

To clarify the relationship between cluster formation and granular flow regime, the maximum flow depth h_{max} is plotted against α shown in Fig. 9. The Pearson coefficient $r \approx 0.86$ implies that the cluster size and flow depth are in a considerable positive correlation relationship. Since the clusters can possess a relatively irregular topology

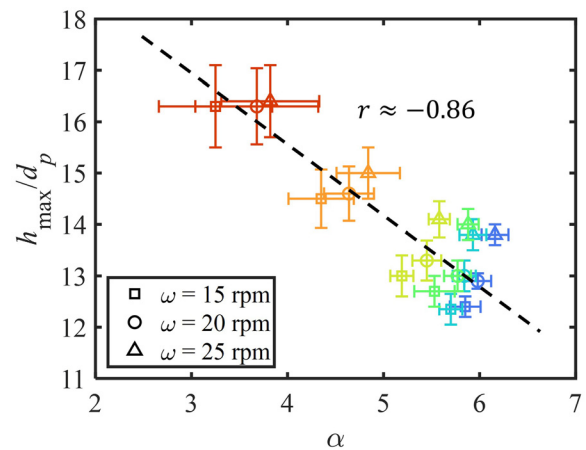


FIG. 9. The max flow depth h_{max} vs cluster size distribution power index α shown in Fig. 8. The dashed line is a line of best fit with correlation coefficient r .

compared to single-sphere particles, higher resistance of inter-cluster contact (higher inter-cluster friction and rolling resistance) can be raised to hinder the relative inter-cluster movement.^{7,76} Moreover, Cao *et al.*²⁵ also mentioned that the inter-cluster and intra-cluster plastic rearrangement can play key roles in dissipating energy in granular flows. In summary, an increase in cohesion is found to induce the granular flow to form relatively larger clusters, which can be the key regime affecting the granular flow.

IV. CONCLUSIONS

In this study, partially saturated granular flow in a rotating drum is studied experimentally and numerically. We first demonstrate that the experimentally observed rolling and cascading modes, controlled by the inter-particle cohesion and drum rotation rate, are successfully captured in the numerical simulation using the discrete element method.

With the combined effects of cohesion, inertia, and gravity, a dimensionless parameter, C_E , is proposed to quantitatively describe the cohesive granular flow. For the first time, a collapse of data on the dynamic angle of repose under different rotation rate and cohesive forces is observed. This implies the capability and universality of the proposed C_E in capturing the interplay among key mechanisms for cohesive granular flows.

At the meso-scale and particle level, the depth of flow region and the statistics of cluster formations in cohesive granular flow are examined. The transition from an inertia-dominated regime to a cohesion-dominated regime is highlighted. We further explored the correlation between the flow depth and cluster formation (with a correlation coefficient > 0.8), showing the effects of the cohesion manifested by the cluster formation.

Our results and analyses shed light on the multiscale connection across the particle-level mechanism, i.e., grain agglomeration, expansion of flow region (meso), and macroscopic observations characterized by the dynamic angle of repose. This study provides a new perspective on cohesive granular flows via revealing the dominating lower-scale features. This could benefit the development of various engineering applications, such as the food industry,^{77,78} mineral handling,^{79,80} and slope analysis under unsaturated conditions.^{81–83}

SUPPLEMENTARY MATERIAL

See the supplementary material for the supplementary figures on the normalized velocity, strain rate, and packing fraction along the flow depth as well as the translational granular temperature diagram.

AUTHOR DECLARATIONS

Conflict of Interest

The authors have no conflicts to disclose.

Author Contributions

Mingrui Dong: Conceptualization (lead); Formal analysis (equal); Methodology (lead); Visualization (lead); Writing – original draft (lead). **Zhongzheng Wang:** Conceptualization (equal); Formal analysis (equal); Methodology (equal); Writing – original draft (equal); Writing – review & editing (equal). **Benjy Marks:** Formal analysis (supporting); Methodology (supporting); Writing – review & editing (supporting). **Yu Chen:** Conceptualization (supporting); Formal analysis (supporting); Writing – review & editing (supporting). **Yixiang Gan:**

Conceptualization (equal); Formal analysis (equal); Methodology (equal); Resources (equal); Supervision (equal); Writing – review & editing (equal).

DATA AVAILABILITY

The data that support the findings of this study are available from the corresponding author upon reasonable request.

REFERENCES

- B. Andreotti, Y. Forterre, and O. Pouliquen, *Granular Media: Between Fluid and Solid* (Cambridge University Press, 2013).
- T. S. Komatsu, S. Inagaki, N. Nakagawa, and S. Nasuno, “Creep motion in a granular pile exhibiting steady surface flow,” *Phys. Rev. Lett.* **86**, 1757 (2001).
- G. MiDi, “On dense granular flows,” *Eur. Phys. J. E* **14**, 341–365 (2004).
- Y. Forterre and O. Pouliquen, “Flows of dense granular media,” *Annu. Rev. Fluid Mech.* **40**, 1–24 (2008).
- H. Norouzi, R. Zarghami, and N. Mostoufi, “Insights into the granular flow in rotating drums,” *Chem. Eng. Res. Des.* **102**, 12–25 (2015).
- E. Espirito, A. Kumar, A. Nommeots-Nomm, J. M. Lerma, and M. Brochu, “Investigation of the rotating drum technique to characterise powder flow in controlled and low pressure environments,” *Powder Technol.* **366**, 925–937 (2020).
- P. G. Rognon, J.-N. Roux, M. Naaïm, and F. Chevoir, “Dense flows of cohesive granular materials,” *J. Fluid Mech.* **596**, 21–47 (2008).
- A. V. Orpe and D. Khakhar, “Scaling relations for granular flow in quasi-two-dimensional rotating cylinders,” *Phys. Rev. E* **64**, 031302 (2001).
- N. Wang, H. Lu, J. Xu, X. Guo, and H. Liu, “Granular flows of binary mixtures down an inclined channel,” *Int. J. Multiphase Flow* **120**, 103097 (2019).
- S. Mandal, M. Nicolas, and O. Pouliquen, “Insights into the rheology of cohesive granular media,” *Proc. Natl. Acad. Sci. U. S. A.* **117**, 8366–8373 (2020).
- D. Bonamy, F. Daviaud, L. Laurent, M. Bonetti, and J.-P. Bouchaud, “Multiscale clustering in granular surface flows,” *Phys. Rev. Lett.* **89**, 034301 (2002).
- A. V. Orpe and D. Khakhar, “Rheology of surface granular flows,” *J. Fluid Mech.* **571**, 1–32 (2007).
- P.-P. Cortet, D. Bonamy, F. Daviaud, O. Dauchot, B. Dubrulle, and M. Renouf, “Relevance of visco-plastic theory in a multi-directional inhomogeneous granular flow,” *Europhys. Lett.* **88**, 14001 (2009).
- A. Jarray, V. Magnanimo, and S. Luding, “Wet granular flow control through liquid induced cohesion,” *Powder Technol.* **341**, 126–139 (2019).
- O. Pouliquen, “Velocity correlations in dense granular flows,” *Phys. Rev. Lett.* **93**, 248001 (2004).
- R. Brewster, G. S. Grest, J. W. Landry, and A. J. Levine, “Plug flow and the breakdown of bagnold scaling in cohesive granular flows,” *Phys. Rev. E* **72**, 061301 (2005).
- F. Da Cruz, S. Emam, M. Prochnow, J.-N. Roux, and F. Chevoir, “Rheophysics of dense granular materials: Discrete simulation of plane shear flows,” *Phys. Rev. E* **72**, 021309 (2005).
- P. Tegzes, T. Vicsek, P. Schiffer *et al.*, “Avalanche dynamics in wet granular materials,” *Phys. Rev. Lett.* **89**, 094301 (2002).
- S. Chou and S. Hsiau, “Experimental analysis of the dynamic properties of wet granular matter in a rotating drum,” *Powder Technol.* **214**, 491–499 (2011).
- M. Renouf, D. Bonamy, F. Dubois, and P. Alart, “Numerical simulation of two-dimensional steady granular flows in rotating drum: On surface flow rheology,” *Phys. Fluids* **17**, 103303 (2005).
- M. Ostoja-Starzewski, “Material spatial randomness: From statistical to representative volume element,” *Probab. Eng. Mech.* **21**, 112–132 (2006).
- T. Qu, Y. Feng, and M. Wang, “An adaptive granular representative volume element model with an evolutionary periodic boundary for hierarchical multiscale analysis,” *Int. J. Numer. Methods Eng.* **122**, 2239–2253 (2021).
- M. Y. Shaheen, A. R. Thornton, S. Luding, and T. Weinhart, “The influence of material and process parameters on powder spreading in additive manufacturing,” *Powder Technol.* **383**, 564–583 (2021).
- W. D. Fullmer and C. M. Hrenya, “The clustering instability in rapid granular and gas–solid flows,” *Annu. Rev. Fluid Mech.* **49**, 485–510 (2017).

- ²⁵Y. Cao, J. Li, B. Kou, C. Xia, Z. Li, R. Chen, H. Xie, T. Xiao, W. Kob, L. Hong *et al.*, "Structural and topological nature of plasticity in sheared granular materials," *Nat. Commun.* **9**, 2911 (2018).
- ²⁶D. Bonamy, F. Daviaud, L. Laurent *et al.*, "Experimental study of granular surface flows via a fast camera: A continuous description," *Phys. Fluids* **14**, 1666–1673 (2002).
- ²⁷Y. Zou, G. Ma, J. Mei, J. Zhao, and W. Zhou, "Microscopic origin of shape-dependent shear strength of granular materials: A granular dynamics perspective," *Acta Geotech.* **17**, 2697–2710 (2022).
- ²⁸H. Henein, J. Brimacombe, and A. Watkinson, "Experimental study of transverse bed motion in rotary kilns," *Metall. Trans. B* **14**, 191–205 (1983).
- ²⁹S. Nowak, A. Samadani, A. Kudrolli *et al.*, "Maximum angle of stability of a wet granular pile," *Nat. Phys.* **1**, 50–52 (2005).
- ³⁰N. Taberlet, P. Richard, and E. J. Hinch, "S shape of a granular pile in a rotating drum," *Phys. Rev. E* **73**, 050301 (2006).
- ³¹M. Arntz, W. K. den Otter, W. J. Briels, P. Bussmann, H. Beftink, and R. Boom, "Granular mixing and segregation in a horizontal rotating drum: A simulation study on the impact of rotational speed and fill level," *AIChE J.* **54**, 3133–3146 (2008).
- ³²R. Brewster, G. S. Grest, and A. J. Levine, "Effects of cohesion on the surface angle and velocity profiles of granular material in a rotating drum," *Phys. Rev. E* **79**, 011305 (2009).
- ³³P. Liu, R. Yang, and A. Yu, "Self-diffusion of wet particles in rotating drums," *Phys. Fluids* **25**, 063301 (2013).
- ³⁴Q. Xu, A. V. Orpe, and A. Kudrolli, "Lubrication effects on the flow of wet granular materials," *Phys. Rev. E* **76**, 031302 (2007).
- ³⁵F. Chen and H. Yan, "Elastic-viscoplastic constitutive theory of dense granular flow and its three-dimensional numerical realization," *Phys. Fluids* **33**, 123310 (2021).
- ³⁶J. Rajchenbach, "Flow in powders: From discrete avalanches to continuous regime," *Phys. Rev. Lett.* **65**, 2221 (1990).
- ³⁷F. Elekes and E. J. Parteli, "An expression for the angle of repose of dry cohesive granular materials on earth and in planetary environments," *Proc. Natl. Acad. Sci. U. S. A.* **118**, e2107965118 (2021).
- ³⁸K. R. Sunkara, F. Herz, E. Specht, and J. Mellmann, "Influence of flight design on the particle distribution of a flighted rotating drum," *Chem. Eng. Sci.* **90**, 101–109 (2013).
- ³⁹L. Zhang, F. Weigler, V. Idakiev, Z. Jiang, L. Mörl, J. Mellmann, and E. Tsotsas, "Experimental study of the particle motion in flighted rotating drums by means of magnetic particle tracking," *Powder Technol.* **339**, 817–826 (2018).
- ⁴⁰C. Feng and A. Yu, "Effect of liquid addition on the packing of mono-sized coarse spheres," *Powder Technol.* **99**, 22–28 (1998).
- ⁴¹M. Scheel, R. Seemann, M. Brinkmann, M. Di Michiel, A. Sheppard, B. Breidenbach, and S. Herminghaus, "Morphological clues to wet granular pile stability," *Nat. Mater.* **7**, 189–193 (2008).
- ⁴²Z. Wang, J.-M. Pereira, and Y. Gan, "Packing of wet monodisperse spheres," *Powder Technol.* **378**, 60–64 (2021).
- ⁴³S. Mutters and K. Rietema, "The effect of interparticle forces on the expansion of a homogeneous gas-fluidized bed," *Powder Technol.* **18**, 239–248 (1977).
- ⁴⁴P. A. Cundall and O. D. Strack, "A discrete numerical model for granular assemblies," *Géotechnique* **29**, 47–65 (1979).
- ⁴⁵O. R. Walton, "Numerical simulation of inclined chute flows of monodisperse, inelastic, frictional spheres," *Mech. Mater.* **16**, 239–247 (1993).
- ⁴⁶S. Luding, "Anisotropy in cohesive, frictional granular media," *J. Phys.* **17**, S2623 (2005).
- ⁴⁷Y. Gan and M. Kamlah, "Discrete element modelling of pebble beds: With application to uniaxial compression tests of ceramic breeder pebble beds," *J. Mech. Phys. Solids* **58**, 129–144 (2010).
- ⁴⁸C. Kloss, C. Goniva, A. Hager, S. Amberger, and S. Pirker, "Models, algorithms and validation for opensource DEM and CFD-DEM," *Prog. Comput. Fluid Dyn.* **12**, 140–152 (2012).
- ⁴⁹N. V. Brilliantov, F. Spahn, J.-M. Hertzsch, and T. Pöschel, "Model for collisions in granular gases," *Phys. Rev. E* **53**, 5382 (1996).
- ⁵⁰K. Iwashita and M. Oda, "Rolling resistance at contacts in simulation of shear band development by dem," *J. Eng. Mech.* **124**, 285–292 (1998).
- ⁵¹J. Ai, J.-F. Chen, J. M. Rotter, and J. Y. Ooi, "Assessment of rolling resistance models in discrete element simulations," *Powder Technol.* **206**, 269–282 (2011).
- ⁵²E. J. Parteli, J. Schmidt, C. Blümel, K.-E. Wirth, W. Peukert, and T. Pöschel, "Attractive particle interaction forces and packing density of fine glass powders," *Sci. Rep.* **4**, 6227 (2014).
- ⁵³R. Yang, R. Zou, and A. Yu, "Computer simulation of the packing of fine particles," *Phys. Rev. E* **62**, 3900 (2000).
- ⁵⁴R. Fuchs, T. Weinhart, J. Meyer, H. Zhuang, T. Staedler, X. Jiang, and S. Luding, "Rolling, sliding and torsion of micron-sized silica particles: Experimental, numerical and theoretical analysis," *Granul. Matter* **16**, 281–297 (2014).
- ⁵⁵H. Tang, R. Song, Y. Dong, and X. Song, "Measurement of restitution and friction coefficients for granular particles and discrete element simulation for the tests of glass beads," *Materials* **12**, 3170 (2019).
- ⁵⁶A. Bhateja, I. Sharma, J. K. Singh *et al.*, "Scaling of granular temperature in vibro-fluidized grains," *Phys. Fluids* **28**, 043301 (2016).
- ⁵⁷C. V. Raman, "The photographic study of impact at minimal velocities," *Phys. Rev.* **12**, 442–447 (1918).
- ⁵⁸C. Thornton and Z. Ning, "A theoretical model for the stick/bounce behaviour of adhesive, elastic-plastic spheres," *Powder Technol.* **99**, 154–162 (1998).
- ⁵⁹C. Sorace, M. Louge, M. Crozier, and V. Law, "High apparent adhesion energy in the breakdown of normal restitution for binary impacts of small spheres at low speed," *Mech. Res. Commun.* **36**, 364–368 (2009).
- ⁶⁰A. Ruiz-Angulo and M. L. Hunt, "Measurements of the coefficient of restitution for particle collisions with ductile surfaces in a liquid," *Granul. Matter* **12**, 185–191 (2010).
- ⁶¹Z. Shi, Y. Zhang, M. Liu, D. A. Hanaor, and Y. Gan, "Dynamic contact angle hysteresis in liquid bridges," *Colloids Surf., A* **555**, 365–371 (2018).
- ⁶²C. K. Lun and S. B. Savage, "The effects of an impact velocity dependent coefficient of restitution on stresses developed by sheared granular materials," *Acta Mech.* **63**, 15–44 (1986).
- ⁶³F. Soulie, F. Cherblanc, M. S. El Youssoufi, and C. Saix, "Influence of liquid bridges on the mechanical behaviour of polydisperse granular materials," *Int. J. Numer. Anal. Methods Geomech.* **30**, 213–228 (2006).
- ⁶⁴C. D. Willett, M. J. Adams, S. A. Johnson, and J. P. Seville, "Capillary bridges between two spherical bodies," *Langmuir* **16**, 9396–9405 (2000).
- ⁶⁵J. H. Snoeijer, J. Eggers, and C. H. Venner, "Similarity theory of lubricated hertzian contacts," *Phys. Fluids* **25**, 101705 (2013).
- ⁶⁶R. Tate, K. Watts, C. Allen, and K. Wilkie, "The viscosities of three biodiesel fuels at temperatures up to 300 °C," *Fuel* **85**, 1010–1015 (2006).
- ⁶⁷G. Lian, C. Thornton, and M. J. Adams, "A theoretical study of the liquid bridge forces between two rigid spherical bodies," *J. Colloid Interface Sci.* **161**, 138–147 (1993).
- ⁶⁸S. R. Jaggannagari, R. K. Desu, J. Reimann, Y. Gan, M. Moscardini, and R. K. Annabattula, "DEM simulations of vibrated sphere packings in slender prismatic containers," *Powder Technol.* **393**, 31–59 (2021).
- ⁶⁹M. Dong, Z. Wang, and Y. Gan, "Wet mono-sized granular packing: Effects of initial clusters and filling strategy," *Powder Technol.* **407**, 117678 (2022).
- ⁷⁰S. He, J. Gan, D. Pinson, A. Yu, and Z. Zhou, "Flow regimes of cohesionless ellipsoidal particles in a rotating drum," *Powder Technol.* **354**, 174–187 (2019).
- ⁷¹P. Liu, R. Yang, and A. Yu, "Dynamics of wet particles in rotating drums: Effect of liquid surface tension," *Phys. Fluids* **23**, 013304 (2011).
- ⁷²K. A. Klise, D. Moriarty, H. Yoon, and Z. Karpyn, "Automated contact angle estimation for three-dimensional x-ray microtomography data," *Adv. Water Res.* **95**, 152–160 (2016).
- ⁷³L. Kovalcinova, S. Karmakar, M. Schaber, A.-L. Schuhmacher, M. Scheel, M. DiMichiel, M. Brinkmann, R. Seemann, and L. Kondic, "Energy dissipation in sheared wet granular assemblies," *Phys. Rev. E* **98**, 032905 (2018).
- ⁷⁴M. Ester, H.-P. Kriegel, J. Sander, X. Xu *et al.*, "A density-based algorithm for discovering clusters in large spatial databases with noise," in *KDD 96* (AAAI Press, 1996), pp. 226–231.
- ⁷⁵J. Murray, S. Benyahia, P. Metzger, and C. Hrenya, "Continuum representation of a continuous size distribution of particles engaged in rapid granular flow," *Phys. Fluids* **24**, 083303 (2012).
- ⁷⁶C. S. Campbell, "Clusters in dense-inertial granular flows," *J. Fluid Mech.* **687**, 341–359 (2011).

- ⁷⁷N. Mitarai and F. Nori, "Wet granular materials," *Adv. Phys.* **55**, 1–45 (2006).
- ⁷⁸J. Mellmann, T. Hoffmann, and C. Fülll, "Mass flow during unloading of agricultural bulk materials from silos depending on particle form, flow properties and geometry of the discharge opening," *Powder Technol.* **253**, 46–52 (2014).
- ⁷⁹S. Lourenço, D. Gallipoli, C. E. Augarde, D. G. Toll, P. C. Fisher, and A. Congreve, "Formation and evolution of water menisci in unsaturated granular media," *Géotechnique* **62**, 193–199 (2012).
- ⁸⁰I. J. Alhani, M. J. b M. Noor, M. A. M. Al-Bared, I. S. H. Harahap, and W. M. Albadri, "Mechanical response of saturated and unsaturated gravels of different sizes in drained triaxial testing," *Acta Geotech.* **15**, 3075–3093 (2020).
- ⁸¹J. W. Godt, R. L. Baum, and N. Lu, "Landsliding in partially saturated materials," *Geophys. Res. Lett.* **36**, L02403, <https://doi.org/10.1029/2008GL035996> (2009).
- ⁸²M. S. Morse, N. Lu, A. Wayllace, J. W. Godt, and W. Take, "Experimental test of theory for the stability of partially saturated vertical cut slopes," *J. Geotech. Geoenviron. Eng.* **140**, 04014050 (2014).
- ⁸³R. Darban, E. Damiano, A. Minardo, L. Olivares, L. Picarelli, and L. Zeni, "An experimental investigation on the progressive failure of unsaturated granular slopes," *Geosciences* **9**, 63 (2019).